



Construction of Z-scheme BiOI/g-C₃N₄ heterojunction with enhanced photocatalytic activity and stability under visible light

Yuzhen Li^{1,2} · Zhen Li¹ · Lizhen Gao^{1,3}

Received: 24 March 2019 / Accepted: 1 June 2019 / Published online: 8 June 2019
© Springer Science+Business Media, LLC, part of Springer Nature 2019

Abstract

BiOI/g-C₃N₄ binary catalysts with different loading ratios were prepared by a mild one-step stirring method. The optimum loading ratio of BiOI was selected by photocatalytic degradation of 20 mg/L methyl orange (MO) under visible light irradiation. The experimental results of photocatalytic degradation of MO indicated that the loading of BiOI improves the photocatalytic performance of g-C₃N₄. The structure and morphology of the catalyst were examined by X-ray diffraction (XRD), transmission electron microscopy (TEM), ultraviolet–visible (UV–vis) diffuse reflectance spectroscopy (DRS), photoluminescence spectroscopy (PL) and fourier transform infrared spectroscopy (FT-IR). The characterization results showed that BiOI and g-C₃N₄ were well complexed together, the Z-type heterojunction between them increased the utilization of visible light by g-C₃N₄ and reduced the recombination rate of photogenerated electron–hole pairs. In addition, the effects of catalyst loading, initial concentration of solution and initial pH on the photocatalytic degradation of MO by BiOI/g-C₃N₄ under visible light were explored. As a result, it was found that the optimum dosage of the binary catalyst was 1.25 g/L, and the photocatalytic efficiency against MO decreased as the initial concentration increased. In addition, the initial pH of the MO solution had a complicated effect on the photocatalytic efficiency of the binary catalyst, which was related to the existence form of MO in different environments. Finally, the main factors of photocatalytic degradation of MO were confirmed by free radical trapping experiments. Based on the results, the possible mechanism of photocatalytic degradation of MO by BiOI/g-C₃N₄ was inferred. Enhanced visible light photocatalytic activity was obtained due to light trapping of photogenerated carriers, high transfer efficiency, and enhanced separation efficiency by Z-type heterojunction.

1 Introduction

The development of science, technology and industry has promoted the progress of society and made people's lives more convenient and faster, but at the same time caused damage to the natural environment and brought about shortage of resources. The serious shortage of clean water and energy has seriously hampered economic and social development [1]. The problem of energy shortage and environmental pollution has become a problem that threatens the

world. In particular, the shortages of water resources and water pollution have already affected people's daily lives. Therefore, how to reduce water pollution has become an issue of concern to all countries.

Organic dyes are toxic contaminants that are commonly found in the waste streams released in textiles, leather, cosmetics, printing, pharmaceuticals, food processing and rubber processing industries [2]. These dyes enter the natural world with the waste water discharged from the factory, and have direct and potential toxicity to humans, animals, plants and aquatic organisms [3]. To remove organic dyes from sewage, many methods are used, such as biological treatment such as activated sludge [4], physical methods such as physical adsorption [5], and chemical methods such as Fenton oxidation [6]. However, these methods have obvious drawbacks. The activated sludge method can only remove waste water with a low concentration of contaminant. The physical method can only remove waste water containing large particles. The operation of the chemical oxidation method is complicated and costly. Therefore, the photocatalytic

✉ Yuzhen Li
liyuzhen123456@126.com; liyuzhen@tyut.edu.cn

¹ College of Environmental Science and Engineering, Taiyuan University of Technology, 79 Yingze Street, Wan bailin District, Taiyuan 030024, China

² China Institute for Radiation Protection, 102 Xuefu Street, Xiaodian District, Taiyuan 030006, China

³ School of Mechanical Engineering, University of Western Australia, 35 Stirling Highway, Perth, WA 6009, Australia

degradation method has attracted people's attention due to its convenient operation, good adaptability to pollutants, and low cost [7, 8].

Since the Japanese scientists Fujishima and Honda discovered in 1972 that the rutile type TiO_2 single crystal electrode was able to decompose water into hydrogen and oxygen at normal temperature and atmospheric pressure [9]. It has also been defined as the beginning of the photocatalysis technology. TiO_2 has high photocatalytic activity, good stability, and low cost, and was considered to be an attractive photocatalytic degradation dye [10]. However, TiO_2 also has defects. First of all, it has low utilization rate of solar light, and its own band gap is wide which reaches 3.2 eV and can only absorb and use ultraviolet light [11]. In addition, its electron hole recombination rate is high, which greatly limits its photocatalytic degradation effect [12].

In order to solve these major defects of TiO_2 , the exploration of photocatalyst based on semiconductor materials has become the theme of people. Among the many photocatalytic materials, $\text{g-C}_3\text{N}_4$ is one of the most interesting catalysts in recent years. It is considered as the next generation photocatalyst in the field of environmental remediation [13]. As a metal free polymer photocatalyst, it shows a series of excellent characteristics, such as high chemical stability and thermal stability, low cost, abundant reserves, flexible supramolecular network, and can easily adjust the properties of the material by exchanging the chemical structure of the skeleton [14, 15]. In addition, because of its narrow band gap (2.7 eV), solar energy can be utilized more efficiently [16].

Although $\text{g-C}_3\text{N}_4$ has excellent catalytic function, at the same time, it also has the disadvantages of high photoelectron-hole pair recombination rate. Therefore, it is necessary to explore how to reduce the photoelectron-hole pair recombination rate and increase its photocatalytic efficiency. The construction of a semiconductor and semiconductor heterojunction can promote the separation of photogenerated electrons and holes, thereby enhancing the photocatalytic performance of semiconductor photocatalysts. A large number of semiconductor materials can be combined with $\text{g-C}_3\text{N}_4$ to form semiconductor heterojunctions, including metal oxides, multi-component oxides, metal oxynitrides, metal sulfides, germanium-based compounds, silver-based compounds, and organic semiconductors [17–21]. Chen et al. [22] used acid-treated $\text{SrWO}_4/\text{g-C}_3\text{N}_4$ as precursor and successfully prepared a novel hierarchical sheet-on-sheet $\text{WO}_3/\text{g-C}_3\text{N}_4$ composite by a simple calcination method. The photocatalytic activity was detected by photocatalytic degradation of rhodamine B under simulated sunlight irradiation. It was found that the degradation rate of rhodamine B by the novel binary materials was 6.5 and 3.0 times than that of monomers WO_3 and $\text{g-C}_3\text{N}_4$, respectively. It is speculated that the photocatalytic activity enhancement of the composite was attributed

to the formation of delaminated heterostructure, which provided a larger specific surface area, better visible light absorption capacity, and reduced photoinduced electron-hole pair recombination and enhanced separation efficiency of charge carriers. Chen et al. [23] used a simple hydrothermal route to in situ MnIn_2S_4 nanosheets on the surface of $\text{g-C}_3\text{N}_4$ to prepare a series of direct Z-scheme $\text{MnIn}_2\text{S}_4/\text{g-C}_3\text{N}_4$ photocatalyst nanosheets without electron media, which can be used to degrade pharmaceutical wastewater and hydrogen generation under visible light. The experimental results showed that these Z-scheme heterostructure photocatalysts exhibit higher photocatalytic activity than single-component samples. The increase of photocatalytic activity was mainly attributed to the construction of Z-scheme $\text{MnIn}_2\text{S}_4/\text{g-C}_3\text{N}_4$ architectures, which effectively accelerated the transfer and separation of photogenerated charge carriers via tight interface contacts built among these two components.

Among many semiconductor materials used for modification, the bismuth salt photocatalyst has high photoelectric conversion efficiency and can achieve high utilization efficiency of sunlight, such as Bi_2WO_6 , BiOBr , BiOI and BiVO_4 are potential photocatalysts with high stability and photocatalytic activity [24–26]. These Bi-based oxides have a hybridized valence band that facilitates the transport of photogenerated holes [27]. At the same time, due to the interaction of the two semiconductors, a high separation rate of photoinduced electron-hole pairs can be achieved [28]. Three element oxide semiconductor, bismuth halide, can effectively induce photoelectron hole pair separation and achieve high photocatalytic performance due to its unique hierarchical structure. Among them, BiOI has the smallest band gap (1.85 eV), which can maximize the use of sunlight [29].

Furthermore, the well-matched band position of $\text{g-C}_3\text{N}_4$ and BiOI was presented, indicated by the highly positive valence band (VB) of BiOI and the highly negative conduction band (CB) of $\text{g-C}_3\text{N}_4$. Through the efficient heterojunction transfer, the corresponding charge carrier lifetime would be significantly prolonged, resulting in an enhanced visible light photocatalytic performance. Thus $\text{BiOI}/\text{g-C}_3\text{N}_4$ binary system was taken into investigation in this work.

Among many organic dyes, methyl orange (MO) is a representative anionic dye which is obtained by coupling diazotization with *p*-aminobenzenesulfonic acid and *N,N*-dimethylaniline. It is commonly used in textiles, laboratory experiments and other commercial products. In addition, due to the different forms of MO in different environments, it is easy to explore the degradation efficiency of photocatalytic materials in different practical situations.

Herein, the research objective of this paper was that $\text{g-C}_3\text{N}_4$ prepared with urea as precursor was selected as the substrate and modified with BiOI . The effect and mechanism

of BiOI/g-C₃N₄ on photocatalytic degradation of organic dyes were investigated using MO as the target pollutant. The optimum loading proportion of BiOI was determined, and on this basis, the amount of catalyst added, the initial concentration and the initial pH of MO were investigated. Finally, the trapping experiment was used to find the active factors that play a major role in the photocatalytic process, and the possible mechanism of photocatalytic degradation of methyl orange was inferred.

2 Experimental section

2.1 Materials

Urea (H₂NCONH₂, 99%) was purchased from Tianjin Damao chemical reagents factory. Bi(NO₃)₃·5H₂O (99%) was provided from Tianjin Kaitong Chemical Reagent Co., Ltd. KI (99%) and MO was supplied from Tianjin Guangfu Technology Development Co., Ltd. Glycol ((CH₂OH)₂) was got from Tianjin Jinfeng Chemical Co., Ltd. Methanol (CH₃OH) and ammonium oxalate (AO) (99.5%) were obtained from Tianjin Zhiyuan Chemical Reagent Co., Ltd. Benzoquinone (BQ) (99%) was purchased from Tianjin Qinghua Jinying Technology Co., Ltd. Tert-butyl alcohol (TBA) was supplied from Tianjin Beichen Founder Reagent Factory. All chemicals were analytical grade and used without further purification. Distilled water was used in the experimental processes.

2.2 Preparation of catalysts

g-C₃N₄ was prepared using urea as a precursor in the previous method [30]. BiOI was prepared by a hydrothermal method [31]. In a typical synthesis, 0.8 mmol of Bi(NO₃)₃·5H₂O was dissolved in 38 mL of glycol to form a solution A with constant stirring. Simultaneously, 0.8 mmol of KI was dissolved into 2 mL of glycol to form a solution B with stirring. Then, the solution B was dropwise at a rate of 10 d/min added into solution A within 30 min stirring, resulting in the formation of mixed solution. The mixture was then transferred to a 50 mL of Teflon lined autoclave. The autoclave was heated at 120 °C for 6 h and then cooled to room temperature. The solid was collected and washed several times with absolute ethanol, then dried at 60 °C for 6 h, and finally the brick red powder was obtained noted as BiOI.

BiOI/g-C₃N₄ was prepared by a mild agitation method. Specifically, 1 g of g-C₃N₄ was added to 50 mL of methanol, placed in an ultrasonic machine for 30 min to disperse it, and then a certain amount of BiOI was added into above solutions and stirred in a fume hood for 24 h until the methanol was volatilized. Finally, the remaining solid was dried at

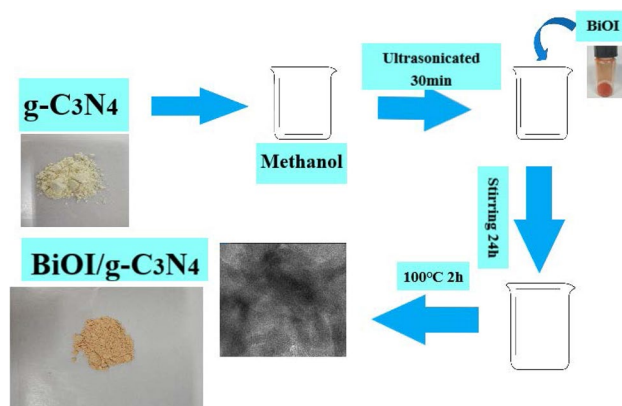
100 °C to obtain BiOI/g-C₃N₄. BiOI/g-C₃N₄ hybrid photocatalysts with different weight ratios of BiOI were prepared. 5% BiOI/g-C₃N₄, 10% BiOI/g-C₃N₄, 15% BiOI/g-C₃N₄, 20% BiOI/g-C₃N₄, 30% BiOI/g-C₃N₄ and 40% BiOI/g-C₃N₄ were prepared and denoted as 5BCN, 10BCN, 15BCN, 20BCN, 30BCN, and 40BCN, respectively. The synthesis process of BiOI/g-C₃N₄ samples was seen in Scheme 1 as the following:

2.3 Characterization

The composition and crystal form of samples were recorded by powder X-ray diffractometer (XRD, LABXRD-6000, Japan) with Cu Kα as a radiation source. The morphology and the size of the as-prepared samples were observed by a JEM-2500SE (Japan) transmission electron microscope (TEM) at an operating voltage of 200 kV. UV-Visible Diffuse Reflectance Spectroscopy (DRS) was tested on a Hitachi SU-3100 spectrophotometer (Japan) using BaSO₄ as a reference. The luminescence properties of the samples were tested using a Shimadzu RF-6000 fluorescence spectrophotometer (PL, Japan) with an excitation wavelength of 380 nm. The structural information of the samples was measured by a Fourier transform spectrophotometer (FT-IR, NICOLET iS10, Thermo Scientific) using a standard KBr disk method. The scanning range was 400 to 4000/cm, the resolution was 4, and the number of scanning times was 20.

2.4 Photocatalytic activity

The experiment selected MO as the target contaminant to detect the photocatalytic property of BiOI/g-C₃N₄. The photodegradation reaction was carried out in a 300 mL reactor and the outside was surrounded with cold water to stabilize the reaction temperature at room temperature. A 300 W xenon lamp with a 420 nm filter was used as the reaction



Scheme 1 Schematic representation of the synthesis process of BiOI/g-C₃N₄ samples

light source. The operating voltage was 14 V and the operating current was 15 A. The distance between the light source and the reactor is 5 cm. The bottom of the reactor is a magnetic stirrer. Magnetron was added in the reactor to facilitate stirring of the solution during the reaction. The concentration of MO was mainly 20 mg/L and 250 mL of solution was used for each degradation test. Each time the catalyst was weighed in a certain proportion, the catalyst is added into the prepared MO solution, and the ultrasound was dispersed for 10 min and then placed in a dark box for dark reaction. After the adsorption–desorption equilibrium is reached, the lamp was turned on for illumination reaction. Samples of 10 mL were taken every 20 min and centrifuged at 10,000 rpm for two more centrifugations every 5 min to ensure complete separation of the catalyst and reaction time is 120 min. The supernatant after separation was tested for absorbance on an ultraviolet–visible spectrophotometer (UV-1800PC). The maximum absorption wavelength of MO was 465 nm.

In addition, to investigating the effect of the loading amount of BiOI on the photocatalytic performance of BiOI/g-C₃N₄, the dosage of the catalyst, the effect of the initial concentration and the initial pH of MO were also explored on the photocatalytic performance. In particular, when exploring the effect of initial pH on photodegradation of MO, HCl and NaOH were selected as the reagents for adjusting the pH of the solution. The effect of catalyst addition on the pH of the solution should be considered before the experiment.

3 Results and discussion

3.1 Enhancement of photocatalytic activity

MO with concentration 20 mg/L was used as the target pollutant to detect the influence of the amount of BiOI loaded in g-C₃N₄ on the degradation of MO. The mass ratios of BiOI selected are 5%, 10%, 15%, 20%, 30% and 40%, respectively. Under the same experimental conditions, the effects of loading amount of BiOI on BiOI/g-C₃N₄ on the degradation of MO were compared.

The photodegradation efficiency of the MO was calculated according to Eq. (1):

$$\eta = \frac{C}{C_0} \quad (1)$$

where: C_0 is the initial concentration of the dye, and C is the concentration of MO after time t . The experimental results are shown in Fig. 1. It can be seen from the diagram that with the increase of BiOI loading amount, the dark adsorption capacity of BiOI/g-C₃N₄ to MO also increased. As the loading ratio of BiOI increased from 0 to 30%, the adsorption amount of catalyst to MO increased from 16.02

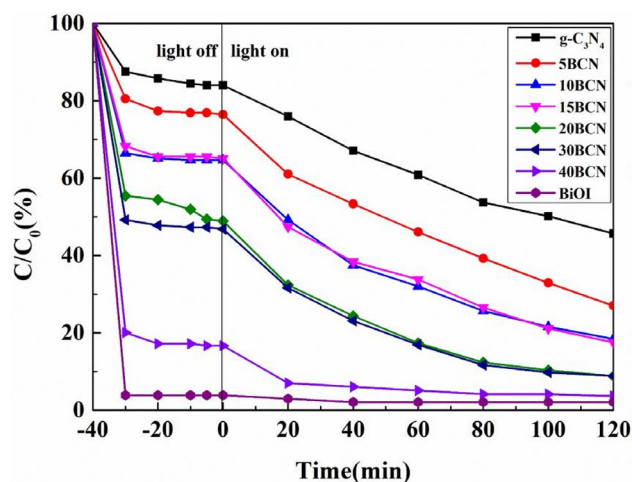


Fig. 1 The photocatalytic efficiency of MO over the g-C₃N₄, 5BCN, 10BCN, 15BCN, 20BCN, 30BCN, 40BCN and BiOI

to 53.17%, and the final decolorization rate of MO solution increased from 54.31 to 91.14%. When the loading ratio of BiOI reached 40%, the dark adsorption capacity of the catalyst to MO is 83.31%, and most of the pollutants were adsorbed, and the final removal effect of photocatalysis was 96.31%. The reason why the amount of dark adsorption increase as the loading amount of BiOI increase was because of the excellent adsorption performance of BiOI for MO. The dark adsorption of pure BiOI to 20 mg/L MO reached 97.11%, and the final removal rate was 97.9%. This meant that the removal of MO by BiOI was mainly by adsorption and did not degrade MO. The dark adsorption of 15BCN compared to BiOI was reduced, and its removal of MO was mainly photocatalytic degradation. The larger dark adsorption of BiOI to MO may be due to its larger specific surface area [32]. In addition, the change in surface charge after g-C₃N₄ was combined with BiOI also leads to an increase in the dark adsorption amount of MO. In order to determine the effect of the amount of BiOI loading on the degradation effect, the following formula was used to calculate the first order rate constant (k_{obs}) of BiOI/g-C₃N₄ with different BiOI loading ratio [33]:

$$k_{obs} = -\frac{1}{t} \ln \left(\frac{C}{C_0} \right) \quad (2)$$

In which, C and C_0 are concentrations of MO in time of t and zero, respectively and the results were shown in Fig. 2. The interaction between g-C₃N₄ and BiOI increased their k_{obs} values. With the increase of BiOI loading (the mass ratios of BiOI from 5 to 20%), the first order rate constant of BiOI/g-C₃N₄ also increased. When the mass ratio of BiOI reached 20%, the first order rate constant of BiOI/g-C₃N₄ degradation of MO reached its peak. And then, with the

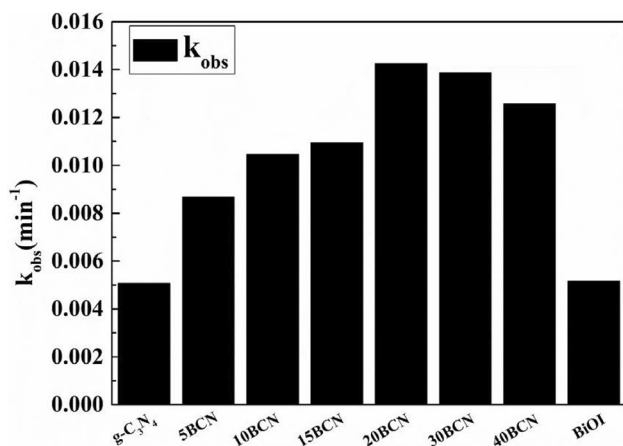


Fig. 2 The degradation rate constant of MO over the $\text{g-C}_3\text{N}_4$, 5BCN, 10BCN, 15BCN, 20BCN, 30BCN, 40BCN and BiOI

increase of BiOI loading ratio (the mass ratios of BiOI from 20 to 40%), the first order rate constant of BiOI/ $\text{g-C}_3\text{N}_4$ degradation of MO began to decrease. This may be because the content of BiOI exceeds 20% amount, the BiOI will decrease the light absorption of $\text{g-C}_3\text{N}_4$, and reduce the rate of generation of photoexcited charge carriers. Another reason may be the dark adsorption amount of BiOI/ $\text{g-C}_3\text{N}_4$ increased as the amount of BiOI doping increased. So the photocatalytic performance is reduced. The k_{obs} of $\text{g-C}_3\text{N}_4$, 5BCN, 10BCN, 15BCN, 20BCN, 30BCN, 40BCN and BiOI were 5.07×10^{-3} , 8.67×10^{-3} , 10.46×10^{-3} , 10.94×10^{-3} , 14.25×10^{-3} , 13.87×10^{-3} , 12.57×10^{-3} and 5.16×10^{-3} min, respectively.

The k_{obs} of 20BCN was the largest, but the dark adsorption of 20BCN to 20 mg/L MO reached 51.08%. In order to reduce the effect of dark adsorption on the photocatalytic effect of BiOI/ $\text{g-C}_3\text{N}_4$, the 15BCN was chosen as the best loading catalyst for subsequent experiments.

3.2 Characterization

3.2.1 Phase structures and morphology

XRD was used to determine the phase structure of the samples. The XRD patterns of $\text{g-C}_3\text{N}_4$, BiOI and 15BCN were shown in Fig. 3. As we can see, pattern of the $\text{g-C}_3\text{N}_4$ sample revealed two distinct diffraction peaks at 27.61° and 12.94° , which could be indexed to the (002) and (100) diffraction planes of the graphite-like carbon nitride [34], and the two peaks correspond to the characteristic interplanar stacking peaks of aromatic systems and interlayer structural packing, respectively, which were the same as in the previous study [35]. On the XRD pattern of BiOI, the strong diffraction angles 2θ at 11.56° , 29.48° , 31.87° , 45.53° and 55.17° could be assigned to the (001), (102),

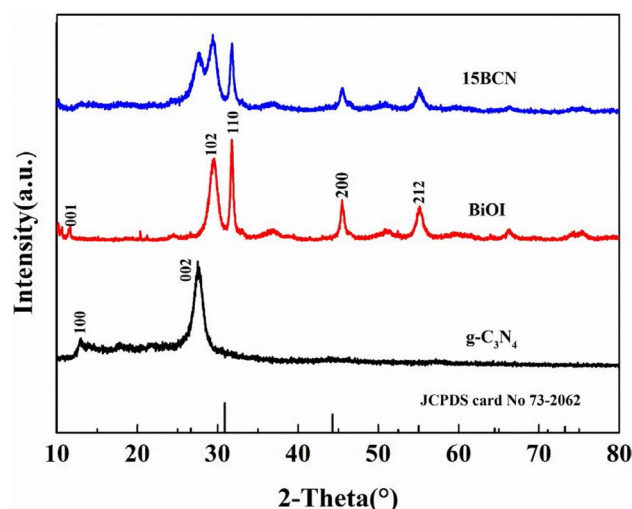


Fig. 3 XRD patterns of $\text{g-C}_3\text{N}_4$, BiOI and 15BCN

(110), (200) and (212) crystal planes of pure BiOI, respectively, which were consistent with the standard card of tetragonal phase BiOI (space group: $p4/nmm$ (129), JCPDS file No. 73-2062). On the XRD pattern of 15BCN, it was found that (002) and (100) diffraction planes corresponding to $\text{g-C}_3\text{N}_4$ and (001), (102), (110), (200) and (212) crystal planes corresponding to BiOI, respectively. And it was found no other peaks, showing that the two materials were well loaded together and the high purity of the as-prepared samples. At the same time, the peaks of the loaded material decreased at each diffraction plane could be clearly seen, the weakening of the peaks might be due to the agglomerate of BiOI [36].

The morphology and microstructure of pure $\text{g-C}_3\text{N}_4$ and the binary 15BCN catalyst was investigated by TEM. Figure 4a, b showed TEM photographs of $\text{g-C}_3\text{N}_4$ and Fig. 4c–f showed TEM photographs of 15BCN. As can be seen from Fig. 4a, b, $\text{g-C}_3\text{N}_4$ was a multi-layered sheet structure, which could increase the specific surface area of catalyst and increase the adsorption capacity, which was consistent with the results shown in Fig. 4c, d. The BiOI particles were attached to the $\text{g-C}_3\text{N}_4$ sheet and had a size of about 50 nm, similar to the study of the former [37]. The high-resolution TEM images of 15BCN were shown in Fig. 4e, f. The d value of 0.302 nm obtained by calculation corresponded to the (102) plane of BiOI [38]. The lattice spacing of $\text{g-C}_3\text{N}_4$ could also be clearly observed and determined to be 0.325 nm, corresponding to the (002) plane [39]. This further showed that BiOI was well attached to $\text{g-C}_3\text{N}_4$, which was consistent with the analysis results of XRD.

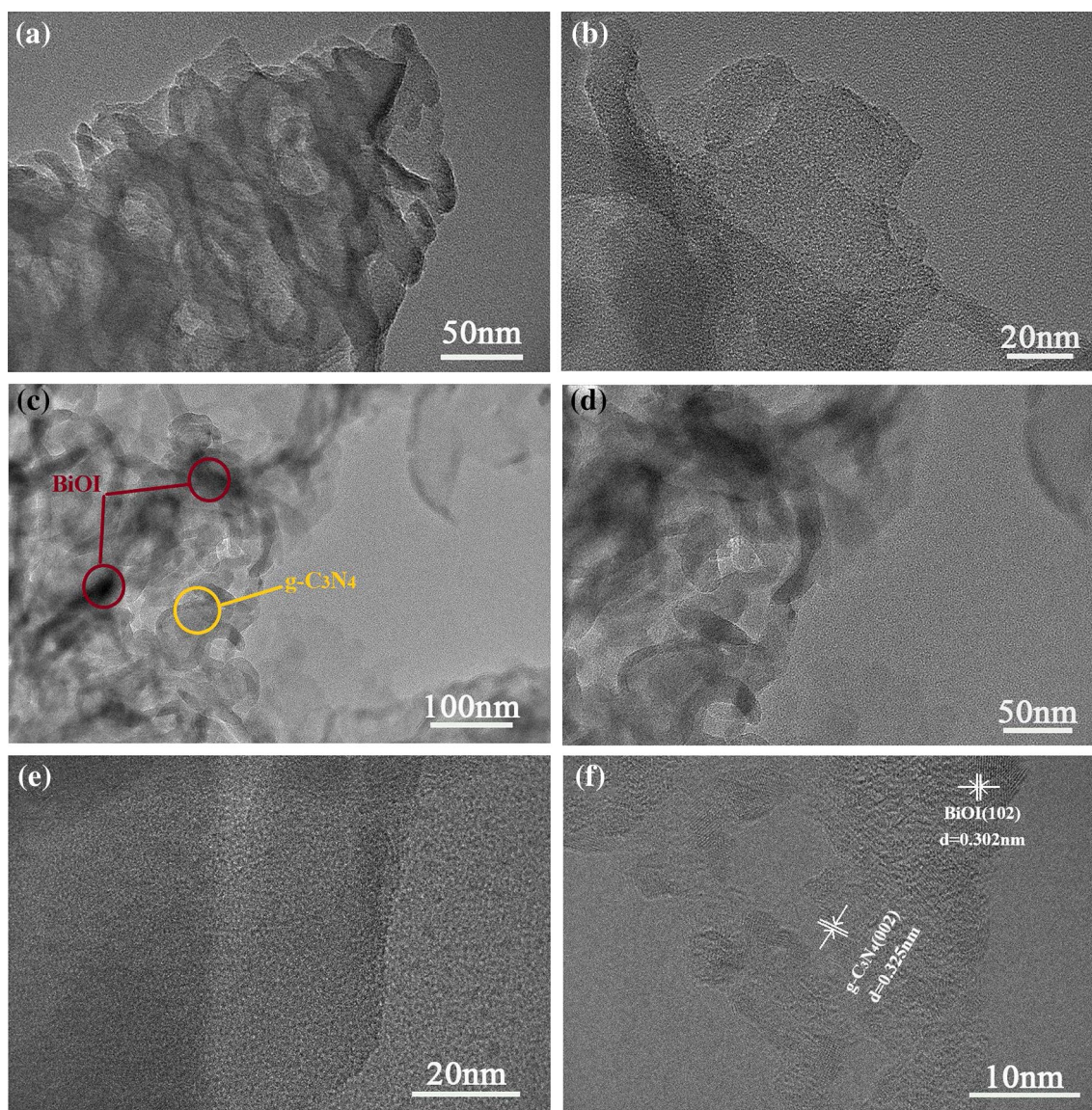


Fig. 4 TEM images of **a, b** $g\text{-C}_3\text{N}_4$ and **c–f** 15BCN

3.2.2 Optical absorption properties

The optical absorption and energy band feature of a semiconductor are important factors determining its photocatalytic performance. The optical absorption properties of $g\text{-C}_3\text{N}_4$, BiOI and 15BCN were detected through UV–Visible diffuse reflectance spectroscopy, and the results were shown in Fig. 5a. It was obvious that the absorption wavelengths of pure $g\text{-C}_3\text{N}_4$, BiOI and 15BCN displayed distinct absorption in the visible-light region. From the Fig. 5, it could be seen that the light absorption band of pure $g\text{-C}_3\text{N}_4$ was around 470 nm, which was the same as the previous report [8]. And the light absorption band of pure BiOI was around 660 nm, which was similar to previous reports [31]. These results showed that they can both absorb and utilize

visible light. Interestingly, the light absorption band of 15BCN had reached about 550 nm, the absorption within the visible light range apparently increased and a red shift appeared compared with that of pure $g\text{-C}_3\text{N}_4$. The absorption intensity of the 15BCN was higher than that of pure $g\text{-C}_3\text{N}_4$ in UV-light region, showing that the preparation of 15BCN could greatly improve the optical absorption property and increase the utilized efficiency of solar light, which were favorable for the enhancement of the photocatalytic activity.

Because of the intensive absorptions in the visible region, the 15BCN nanocomposites could have remarkable photocatalytic activity under the visible-light irradiation. The band gap energy of the prepared catalysts could be calculated by the following formula:

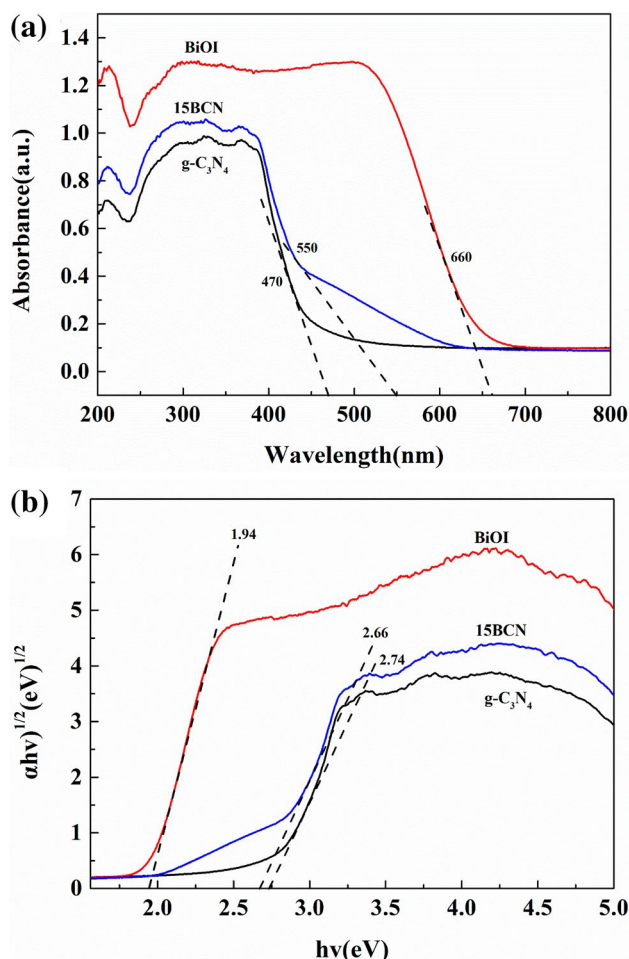


Fig. 5 **a** UV-vis diffuse reflectance spectra and **b** plots of $(ah\nu)^{1/2}$ vs. $h\nu$ of $g\text{-C}_3\text{N}_4$, BiOI and 15BCN

$$\alpha h\nu = A(h\nu - E_g)^{\frac{n}{2}} \quad (3)$$

where: α is the absorption coefficient and E_g is energy band gap of the samples, h , ν and A are the planck constant, optical frequency and constant, respectively. n depends on the characteristics of the transition in a sample (direct transition: $n = 1$; indirect transition: $n = 4$). Pure $g\text{-C}_3\text{N}_4$ and pure BiOI are both indirect semiconductors, and their values of n are 4 [40, 41]. The E_g values are estimated by extrapolation of the linear part of the curves obtained by plotting $(ah\nu)^{1/2}$ versus $h\nu$, as shown in Fig. 5b. From the Fig. 5b, it was notable that the band gaps of $g\text{-C}_3\text{N}_4$ and BiOI were 2.74 eV and 1.94 eV, respectively, which were similar to the results of previous reports [42, 43]. The band gap of 15BCN was 2.66 eV, and the band gap was narrowed by about 0.08 eV compared with pure $g\text{-C}_3\text{N}_4$, which reduced the barrier height to be overcome in the transfer of internal electrons, accelerated the electron transfer inside the catalyst, and prolonged the lifetime of electron-hole pairs, which subsequently resulted in

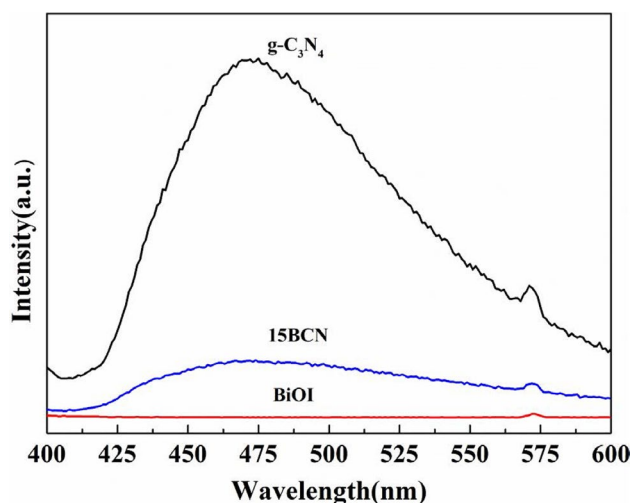


Fig. 6 PL spectra under the excitation wavelength of $g\text{-C}_3\text{N}_4$, BiOI and 15BCN excited by 380 nm

an enhanced photocatalytic activity. The valence band (VB) potential of all samples could be calculated theoretically by the following formula [44]:

$$E_{VB} = X - E^c + 0.5E_g \quad (4)$$

Among them, E_{VB} is the valence band potential of the sample. X is the electronegativity of the sample, which is the geometric mean of the electronegativity of the constituent atoms. E^c is the energy of the free electrons on the hydrogen scale (about 4.5 eV Vs NHE) [31]. E_g is the band gap energy of the sample. By querying, the electronegativity of $g\text{-C}_3\text{N}_4$ and BiOI were 4.72 eV and 6.21 eV, respectively. Therefore, by calculated that the valence band potentials of $g\text{-C}_3\text{N}_4$ and BiOI were 1.59 eV and 2.68 eV, respectively. The conduction band edge potential (E_{CB}) could be calculated by $E_{CB} = E_{VB} - E_g$ and the E_{CB} of $g\text{-C}_3\text{N}_4$ and BiOI were -1.15 eV and 0.74 eV, respectively. These results were similar to previous reports [11, 45, 46].

In order to reflect the transition and separation rate of photogenerated electron-hole pairs, the samples were tested using fluorescence spectrophotometer with an excitation wavelength of 380 nm which were shown in Fig. 6. The lower PL intensity indicated that the charge separation of photogenerated electron-hole pairs was better, because the observed PL emission peaks were attributed to the radiation recombination process of any self-trapping exciton [37]. As can be seen from the Fig. 6, the spectrum of $g\text{-C}_3\text{N}_4$ showed a strong intensity of emission peak at 475 nm, indicating rapid recombination of electrons and holes. The intensity of the emission peak of BiOI at the same position was very low, which indicated that BiOI had an ultra-low electron-hole recombination rate. For the 15BCN binary photocatalyst, it could be seen from Fig. 6 that the intensity of the emission

peak at the same position was significantly lower than that of $g\text{-C}_3\text{N}_4$. This indicated that the photogenerated electron–hole pairs of the composite catalysts were effectively separated, the recombination rate was reduced, and the electron–hole pairs had a longer life. These results were different from the usual PL measurement results and they showed that the photoexcited carriers in the 15BCN hybrid migrated according to a Z-scheme transfer mechanism. Under visible light irradiation, both BiOI and $g\text{-C}_3\text{N}_4$ were excited, and photogenerated electrons on their VB were transferred to their CB, leaving holes on VB. The electrons on the CB of BiOI and the holes on the VB of $g\text{-C}_3\text{N}_4$ recombined to produce a relatively high PL emission intensity, in which strongly reduced electrons on the CB of $g\text{-C}_3\text{N}_4$ and strong oxidized holes on the VB of BiOI participated in the photocatalytic reaction [47]. It could be proved that the heterojunction of BiOI and $g\text{-C}_3\text{N}_4$ can serve as an active center for reducing the photoelectron-hole pair recombination, thereby improving the photocatalytic efficiency of the catalyst. The results of the photoluminescence spectroscopy also confirmed that the results obtained by the UV–visible diffuse reflectance spectra were correct.

3.2.3 FT-IR spectra analysis

To further determine the presence of the different chemical functional groups of the samples. $g\text{-C}_3\text{N}_4$ and 15BCN were characterized by FT-IR spectroscopy, and the FT-IR analysis results of the samples were shown in Fig. 7. It could be seen from the FT-IR spectrum of $g\text{-C}_3\text{N}_4$ that the characteristic peaks were mainly concentrated in the range of 500–1700/cm. The peaks at 1247, 1334, 1414, 1568 and 1642/cm corresponded to the typical stretching mode of the C–N heterocycle [48]. In addition, a peak at 3164/cm could be clearly observed, which corresponded to the stretching mode of

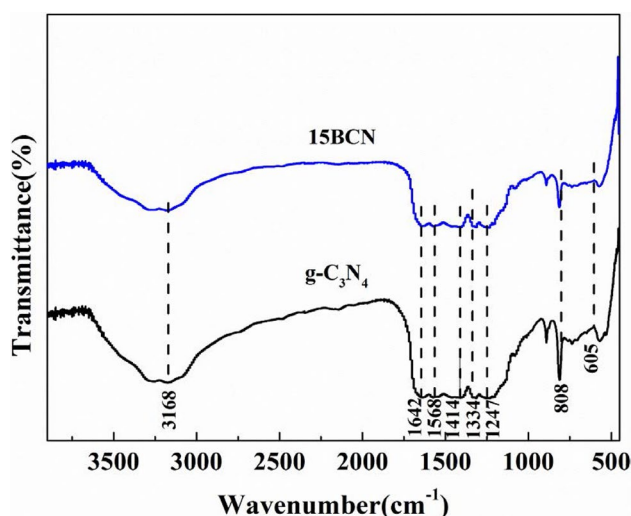


Fig. 7 FT-IR spectra of $g\text{-C}_3\text{N}_4$ and 15BCN

–NH [49]. The characteristic peak at 808/cm belonged to the stretching vibration mode of the thiazine ring unit from $g\text{-C}_3\text{N}_4$ [50]. These indicated that the purity of the monomer $g\text{-C}_3\text{N}_4$ was high. The characteristic peaks of monomeric $g\text{-C}_3\text{N}_4$ were also found on the FT-IR spectrum of 15BCN. What's more, a peak different from the monomer $g\text{-C}_3\text{N}_4$ was found at 605/cm, which was attributed to Bi–O stretching [51]. The pattern indicated that BiOI was successfully combined with $g\text{-C}_3\text{N}_4$. The loading of BiOI resulted in a relative decrease in the $g\text{-C}_3\text{N}_4$ peak, but the characteristic peak of $g\text{-C}_3\text{N}_4$ did not move after binding with the BiOI nanoparticles. This indicated that no covalent bond was formed between BiOI and $g\text{-C}_3\text{N}_4$ [52].

3.3 Photocatalytic activity

3.3.1 Effect of catalyst dosage on the degradation of MO

To study the effect of photocatalysts dosage on degradation efficiency of MO, the experiments were performed by varying amount of 15BCN from 0.25 to 1.5 g/L. The results were shown in Fig. 8. As depicted in Fig. 8, it could be seen that when the dosages were 0.25 g/L and 0.5 g/L, respectively, their dark adsorption amounts of MO were basically same, and the dark adsorption amounts of both were about 7%. Then, with the dosage of 15BCN being 0.75 g/L, 1.00 g/L, 1.25 g/L and 1.50 g/L, the dark adsorption capacity of the catalyst began to increase, which were 16.77%, 19.75%, 26.51% and 29.64%, respectively. The increase of dark adsorption capacity of MO by 15BCN may be due to the increase of total specific surface area caused by the increase of catalyst amount. In addition, with the increase of 15BCN dosage from 0.25 to 1.25 g/L, the final degradation efficiency of MO also increased from 25.5 to 74.08%. This may be due to the amounts of active sites of the catalyst

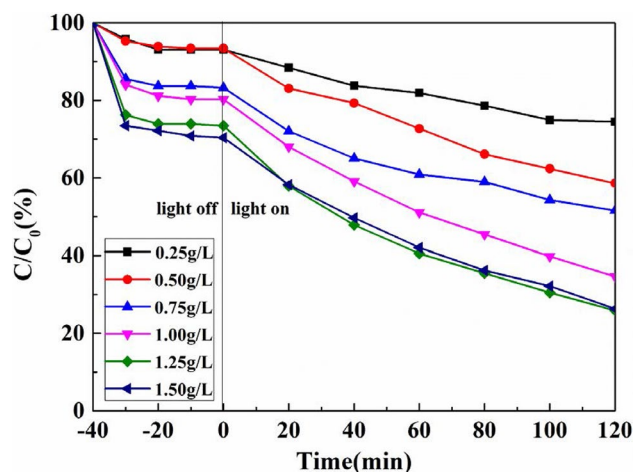


Fig. 8 The photocatalytic efficiency of MO over the 15BCN with different dosages

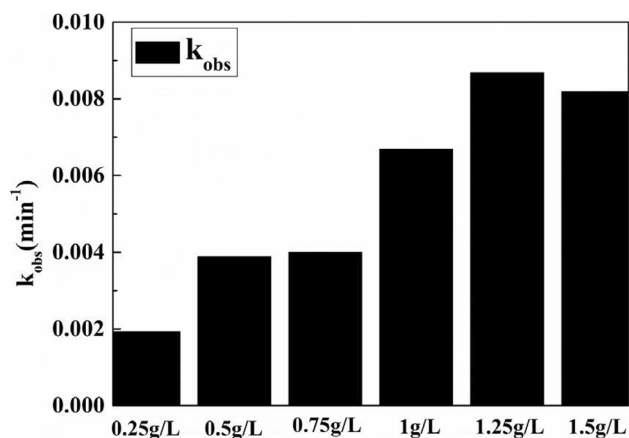


Fig. 9 The degradation rate constant of MO over the 15BCN with different dosages

to generate reactive radicals increased with the increase of catalyst dosage. When the dosage of 15BCN increased from 1.25 g/L to 1.5 g/L, the final degradation effect of MO decreased from 74.08 to 73.65%. This may be due to the increase of the dosage of the catalyst to increase the turbidity of the MO solution, and to influence the absorption of the visible light by the catalyst at the bottom of the solution, thus reducing the degradation efficiency of the MO [52]. The k_{obs} degradation of MO by different dosage (see Fig. 9) showed the same conclusion. When the dosages of 15BCN were 0.25 g/L, 0.5 g/L, 0.75 g/L, 1.0 g/L, 1.25 g/L and 1.5 g/L, k_{obs} were 1.94×10^{-3} and 3.88×10^{-3} , 3.99×10^{-3} , 6.68×10^{-3} , 8.68×10^{-3} and $8.18 \times 10^{-3}/\text{min}$, respectively. As the dosage of 15BCN increased, k_{obs} also increased with the 15BCN degradation of MO, reaching the peak when the dosage reached 1.25 g/L, and then began to decline. Therefore, 1.25 g/L was chosen as the best dosage of 15BCN for photocatalytic degradation of 20 mg/L MO.

3.3.2 Effect of initial concentration on the degradation of MO

In daily life, the concentration of organic dyes in wastewater discharged from factories is uncertain, so it is necessary to explore the degradation effect of 15BCN on MO with different concentrations. The initial concentrations of MO were 5 mg/L, 10 mg/L, 15 mg/L, 20 mg/L and 25 mg/L, respectively, and the effect of MO concentration on degradation

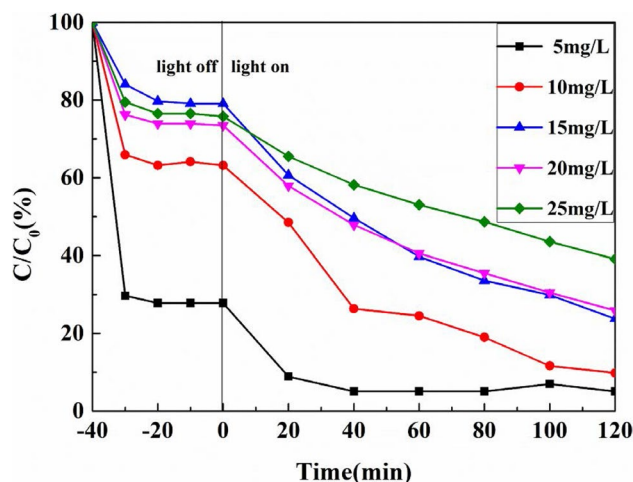
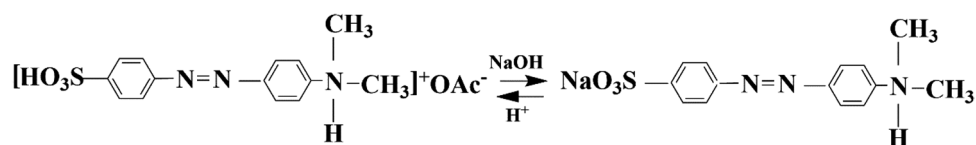


Fig. 10 The photocatalytic efficiency of MO at different initial concentrations over the 15BCN

was investigated by adding 15BCN of 1.25 g/L. With the increase of MO concentration, the amount of dark adsorption also increased. When the initial concentration of MO increased from 5 mg/L to 25 mg/L, the dark adsorption capacity of 15BCN also increased from 3.558 mg/L to 6.18 mg/L. This trend may be explained by the fact that the initial dye concentration provided the sufficient force for mass transfer from the aqueous phase to the solid phase [53]. As shown in Fig. 10, the degradation effect of 15BCN decreased with the increase of initial concentration of MO. After 2 h, the degradation rates of 5 mg/L, 10 mg/L, 15 mg/L, 20 mg/L and 25 mg/L MO were 94.94%, 90.18%, 76.24%, 74.08% and 60.88%, respectively. The increase of initial MO concentration would decrease the probability of reaction between the dye molecules and reactive species [54]. Thus, the degradation efficiency of 15BCN photodegradation was reduced.

3.3.3 Effect of initial pH on the decolorization of MO

pH has great influence on the properties of dyes. Different pH conditions have different forms of dyes, which will also affect the degradation efficiency of the catalysts. In order to explore the degradation effect of 15BCN under different pH conditions, MO was usually used as an indicator of acid and base, because it existed in different forms in different pH conditions and showed different colors. The principle of change was as follows:



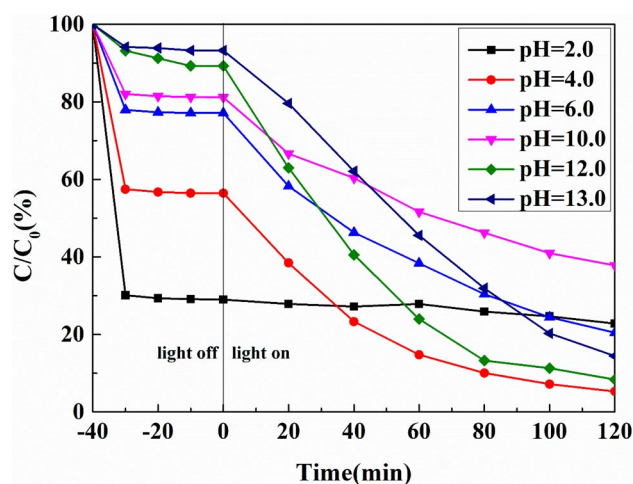


Fig. 11 The photocatalytic efficiency of MO at different initial pH over the 15BCN

MO exhibited azo form under alkaline conditions and quinoid form under acidic conditions. The acidity and basicity of MO had different colors and absorption spectra. In order to compare the above, the absorbance of acid and alkaline MO was superimposed by spectrophotometric method, and the wavelength of the equal absorption point was obtained according to the maximum absorption wavelength of acid and the maximum absorption wavelength of alkali. It was concluded that the wavelength of the equal absorption point of MO was 470 nm. The degradation effect of MO under different pH conditions was determined at the wavelength of equal absorption point. The pH values were selected with 2.0, 4.0, 6.0, 10.0, 12.0, and 13.0, respectively and the pH value of MO solution was adjusted well before the catalyst was added. The results were shown in Fig. 11.

It could be clearly seen that the acidic environment facilitated the dark adsorption of MO by 15BCN. The smaller the initial pH of the solution, the greater the dark adsorption capacity of 15BCN for MO. When pH=2.0, 4.0, 6.0, 10.0, 12.0, and 13.0, the dark adsorption amounts of 15BCN were 70.99%, 43.56%, 22.86%, 18.81%, 10.72% and 7.78%, respectively. This was due to the more positive charge on the surface of the catalyst under the acidic condition, which made it to be easier to form a hydrogen bond with the MO molecule. In addition, due to the high acidity of the SO_3H group, even in the form of deprotonated SO_3^- under high acid conditions, the function of the deprotonated SO_3^- in MO and the positive charge on the surface of the catalyst also caused the increase of the 15BCN dark adsorption capacity.

Finally, the $\text{pK}_a=3.7$ of MO was mainly zwitterionic in the pH acidic range below pK_a , which would also increase the dark adsorption capacity of the catalyst [55]. When pH

value was 2.0, the decolorization rate of MO increased from 70.99 to 77.18% during 120 min, and the MO concentration removed by photodegradation only accounted for 6.17% of the original concentration. On the contrary, under the strong alkaline condition, the dark adsorption capacity of 15BCN to MO was very small, and the photodegradation efficiency was very high. When pH value was 12.0, the decolorization rate of 15BCN on MO increased from 10.72 to 91.62%, and the MO concentration removed by photodegradation accounted for 80.9% of the original concentration. This may be due to the negative charge on the surface of the catalyst under the strong alkaline condition, and the O_2 in MO solution captured a large number of negative charges to generate a large number of $\cdot\text{O}_2^-$, which greatly accelerated the efficiency of MO photodegradation [56]. When pH value was 13.0, the decolorization rate of 15BCN on MO was 85.56%, and the MO concentration removed by photodegradation accounted for 78.78% of the original concentration. This indicated that the photocatalytic effect of 15BCN reached equilibrium after pH = 12.0.

The k_{obs} value of photocatalytic degradation of MO by 15BCN under different pH conditions was shown in Fig. 12. The k_{obs} values at pH=2.0, 4.0, 6.0, 10.0, 12.0, and 13.0 were 2×10^{-3} , 19.7×10^{-3} , 11.05×10^{-3} , 6.37×10^{-3} , 19.72×10^{-3} , and $15.45 \times 10^{-3}/\text{min}$, respectively. It could be seen from the Fig. 12 that the order of the k_{obs} values of photocatalytic degradation of MO by 15BCN at different pH values was: pH = 12.0 \approx pH = 4.0 > pH = 13.0 > pH = 6.0 > pH = 10.0 > pH = 2.0. The first order rate constant at pH = 12.0 was 9.86 times as much as that of pH = 2.0.

3.4 Proposed mechanism

In order to investigate the reaction of active substances in the process of photocatalytic degradation of MO by 15BCN, the free radical capture experiment was used to determine the

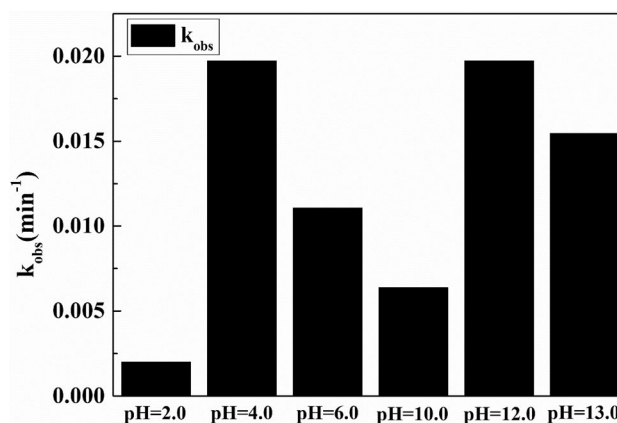


Fig. 12 The degradation rate constant of MO at different initial pH over the 15BCN

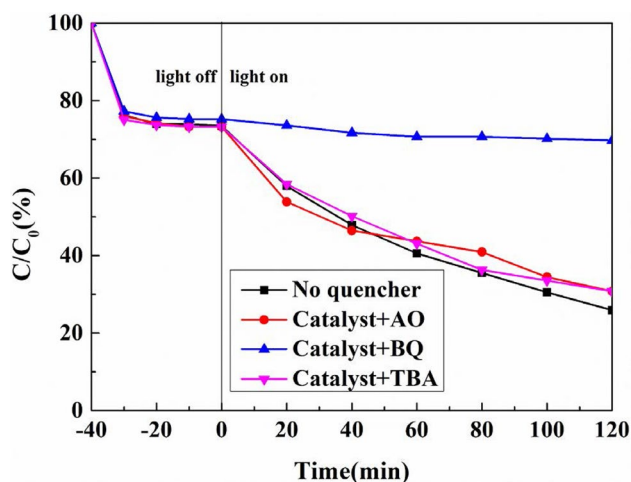


Fig. 13 The photocatalytic efficiency of MO over the 15BCN with different radical scavengers

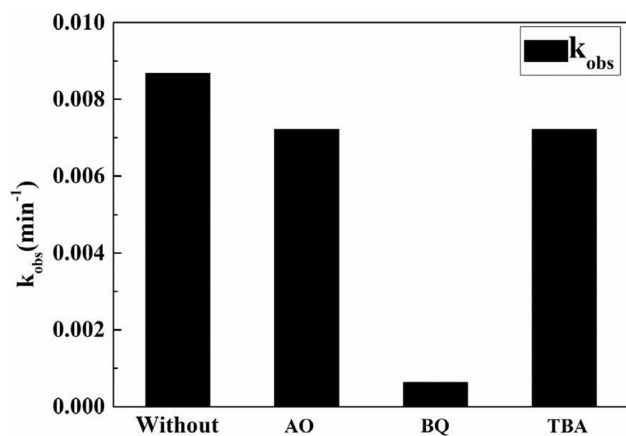


Fig. 14 The degradation rate constant of MO over the 15BCN with different radical scavengers

active factors in the photocatalytic process. The TBA, AO and BQ were used as the hydroxyl radical ($\cdot\text{OH}$) scavenger, hole (h^+) scavenger and superoxide radical ($\cdot\text{O}_2^-$) scavenger, respectively. The trap capture experiment results were shown in Fig. 13. It could be seen from the Fig. 13 that by adding AO to remove holes (h^+), the final result of photocatalytic degradation of MO by 15BCN was reduced from 74.08% to 69.32%, which is reduced by 4.76%, and the amount of change is not large. This indicated that the role of holes in photocatalytic degradation was not significant. Similarly, the final result obtained by the addition of TBA to remove hydroxyl radicals ($\cdot\text{OH}$) was the same that of the addition of AO, indicating that $\cdot\text{OH}$ did not play a major role in photocatalytic degradation. Finally, the superoxide radical ($\cdot\text{O}_2^-$) was removed by the addition of BQ. As a result, the photocatalytic degradation of MO by 15BCN was almost stopped

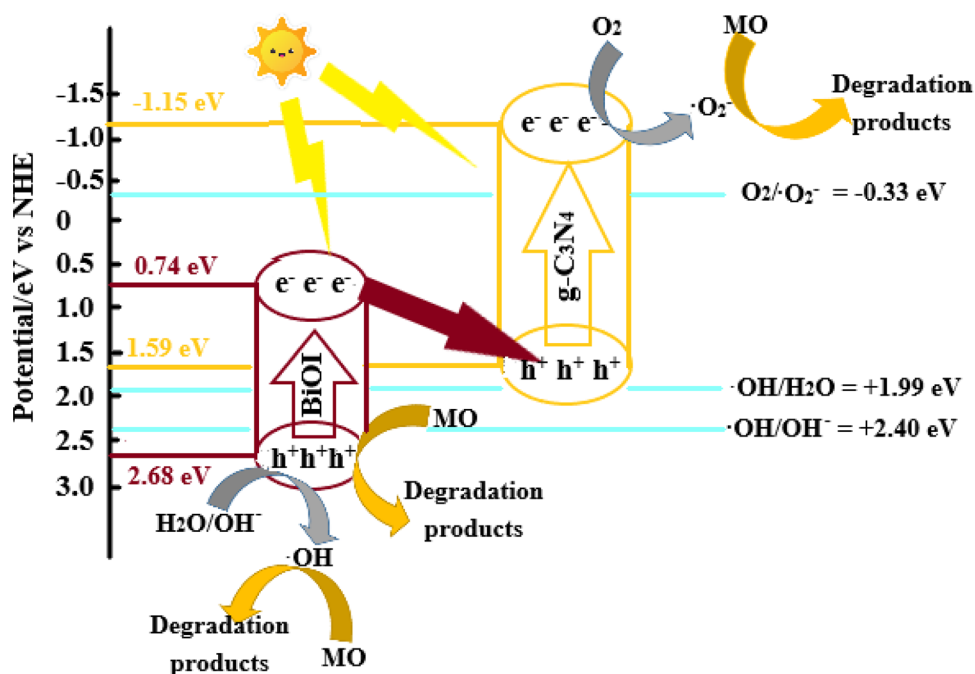
after the dark reaction, the final degradation effect of light for 2 h was reduced from 74.08 to 30.3%, and the degradation rate was reduced by 43.78%, which clearly indicated that $\cdot\text{O}_2^-$ was the main active material in the degradation of MO by 15BCN.

The k_{obs} values in the trap experiment with the addition of various capture agents were shown in Fig. 14. In the absence of any capture agent, the k_{obs} of 15BCN photocatalytic degradation of MO was $8.68 \times 10^{-3}/\text{min}$. With the addition of AO, BQ and TBA, the k_{obs} of photocatalytic degradation of MO by 15BCN were 7.22×10^{-3} , 0.634×10^{-3} and $7.22 \times 10^{-3}/\text{min}$, respectively. The k_{obs} in the case where no capturing agent was added were 1.20, 13.69 and 1.20 times of k_{obs} in the case where AO, BQ and TBA were added, respectively.

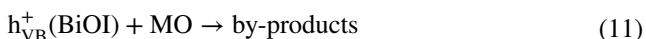
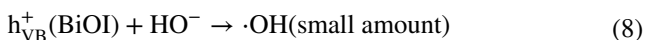
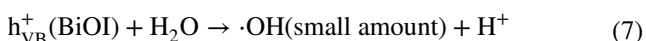
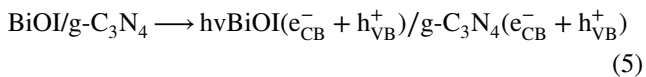
Based on the above experimental results, the possible mechanism of 15BCN photocatalytic degradation of MO was inferred which was shown in Fig. 15. According to the results of DRS, the band gap of BiOI was 1.94 eV (Vs NHE), its valence band (VB) position was 2.68 eV, and its conduction band (CB) position was 0.74 eV. The bandgap of $\text{g-C}_3\text{N}_4$ was 2.74 eV (Vs NHE), its VB position was 1.59 eV, and its CB position was -1.15 eV. Under visible light illumination, when the energy of light radiation is higher than the energy of the catalyst band gap, the catalyst will be excited. Both $\text{g-C}_3\text{N}_4$ and BiOI could be excited by visible light, and electrons (e^-) on their VB received energy to transition to CB and left holes (h^+) on VB. Since the VB potential of $\text{g-C}_3\text{N}_4$ (1.59 eV Vs NHE) is much lower than the potential required to form $\cdot\text{OH}$ ($\cdot\text{OH}/\text{H}_2\text{O} = +1.99$ eV Vs NHE, $\cdot\text{OH}/\text{OH}^- = +2.40$ eV Vs NHE), the h^+ accumulated in the VB of $\text{g-C}_3\text{N}_4$ could not react with the H_2O molecule and OH^- in the solution to form $\cdot\text{OH}$. While the h^+ on the VB of BiOI could react with the H_2O molecule and OH^- in the solution to form $\cdot\text{OH}$. However, due to the small loading ratio of BiOI, this part of $\cdot\text{OH}$ did not play a key role in the photocatalysis process.

This was consistent with the conclusion of the trap experiment. The modification of $\text{g-C}_3\text{N}_4$ by BiOI could be explained by the following mechanism: BiOI formed a Z-type heterojunction with $\text{g-C}_3\text{N}_4$ (Fig. 15). Due to the difference between VB and CB of BiOI and $\text{g-C}_3\text{N}_4$, the CB potential of $\text{g-C}_3\text{N}_4$ is more negative than the CB potential of BiOI, while the VB edge of BiOI is more positive than the VB edge of $\text{g-C}_3\text{N}_4$. So, the e^- on the CB of BiOI and the h^+ on VB of $\text{g-C}_3\text{N}_4$ recombined rapidly, which resulted in the existence of e^- on the CB of $\text{g-C}_3\text{N}_4$. Longer and more likely to react with O_2 to produce more $\cdot\text{O}_2^-$, which in turn promoted photocatalytic degradation of MO. The h^+ remaining on the VB of BiOI and the small amount of $\cdot\text{OH}$ formed by the reaction did not play a major role in the photocatalytic

Fig. 15 The possible degradation mechanism of MO over the 15BCN



process. The specific reaction process is shown in the following formula:



4 Conclusion

In this work, a BiOI/g-C₃N₄ binary catalyst was successfully prepared using a simple one-step stirring method. By photocatalytic degradation of 20 mg/L MO under visible light irradiation, an optimum loading ratio of BiOI of 15% was obtained. Compared with pure g-C₃N₄, 15BCN prepared after loading a small amount of BiOI had a larger dark adsorption amount and a higher photocatalytic efficiency to MO. The first order rate constant of 15BCN degrading 20 mg/L of MO was 2.16 and 2.12 times that of g-C₃N₄ and BiOI, respectively. Through comparison experiments, the optimum dosage of photocatalytic

degradation of 20 mg/L MO was 1.25 g/L. The effect of pH on the catalytic results was complicated. Finally, the free radical capture experiment showed that the active factor that played a major role in the photocatalytic process was superoxide radical ($\cdot\text{O}_2^-$). From the above, the possible photocatalytic mechanism was proposed. In short, the electron transfer of the two materials increased the lifetime of the electron-hole pairs of the catalyst, thereby improving the photocatalytic performance of the catalyst.

Acknowledgements The authors are grateful for financial support from the Shanxi Provincial Key Research and Development Plan (general) Social Development Project (201703D321009-5).

References

1. B. Ge, L. Han, X. Liang, F. Li, X. Pu, X. Zhu, Z. Zhang, X. Shao, C. Jin, W. Li, Fabrication of superhydrophobic Cu-BiOBr surface for oil/water separation and water soluble pollutants degradation. *Appl. Surf. Sci.* **462**, 583–589 (2018)
2. I. Morosanu, C. Teodosiu, A. Coroaba, C. Paduraru, Sequencing batch biosorption of micropollutants from aqueous effluents by rapeseed waste: experimental assessment and statistical modeling. *J. Environ. Manage.* **230**, 110–118 (2019)
3. V.K. Gupta, R. Jain, A. Mittal, T.A. Saleh, A. Nayak, S. Agarwal, S. Sikarwar, Photo-catalytic degradation of toxic dye amaranth on TiO₂/UV in aqueous suspensions. *Mater. Sci. Eng. C.* **32**, 12–17 (2012)
4. M. Bilal, H.M.N. Iqbal, H. Hu, W. Wang, X. Zhang, Enhanced bio-catalytic performance and dye degradation potential of chitosan-encapsulated horseradish peroxidase in a packed bed reactor system. *Sci. Total Environ.* **575**, 1352–1360 (2017)
5. L. Liu, R. Wang, J. Yu, L. Hu, Z. Wang, Y. Fan, Adsorption of Reactive Blue 19 from aqueous solution by chitin nanofiber-/

- nanowhisker-based hydrogels. *RSC Adv.* **8**, 15804–15812 (2018)
6. A.A. Oladipo, A.O. Ifebajo, M. Gazi, Magnetic LDH-based CoO–NiFe₂O₄ catalyst with enhanced performance and recyclability for efficient decolorization of azo dye via Fenton-like reactions. *Appl. Catal. B* **243**, 243–252 (2019)
 7. Y. Chen, W. Huang, D. He, S. Yue, H. Hong, Construction of heterostructured g-C₃N₄/Ag/TiO₂ microspheres with enhanced photocatalysis performance under visible-light irradiation. *ACS Appl. Mater. Interfaces* **6**, 14405–14414 (2014)
 8. M. Xu, L. Han, S. Dong, Facile fabrication of highly efficient g-C₃N₄/Ag₂O heterostructured photocatalysts with enhanced visible-light photocatalytic activity. *ACS Appl. Mater. Interfaces* **5**, 12533–12540 (2013)
 9. A. Fujishima, K. Honda, Electrochemical photolysis of water at a semiconductor electrode. *Nature* **238**, 37–38 (1972)
 10. W. Liang, G. Tang, H. Zhang, C. Li, H. Li, H. Tang, Core-shell structured AgBr incorporated g-C₃N₄ nanocomposites with enhanced photocatalytic activity and stability. *Mater. Technol.* **32**, 675–685 (2017)
 11. C. Chang, L. Zhu, S. Wang, X. Chu, L. Yue, Novel mesoporous graphite carbon nitride/bioi heterojunction for enhancing photocatalytic performance under visible-light irradiation. *ACS Appl. Mater. Interfaces* **6**, 5083–5093 (2014)
 12. X. Guo, X. Li, L. Qin, S.-Z. Kang, G. Li, A highly active nano-micro hybrid derived from Cu-bridged TiO₂/porphyrin for enhanced photocatalytic hydrogen production. *Appl. Catal. B* **243**, 1–9 (2019)
 13. X. Wang, K. Maeda, A. Thomas, K. Takanabe, G. Xin, J.M. Carlsson, K. Domen, M. Antonietti, A metal-free polymeric photocatalyst for hydrogen production from water under visible light. *Nat. Mater.* **8**, 76–80 (2009)
 14. B.V. Lotsch, M. Döblinger, J. Sehnert, L. Seyfarth, J. Senker, O. Oeckler, W. Schnick, Unmasking melon by a complementary approach employing electron diffraction, solid-state NMR spectroscopy, and theoretical calculations-structural characterization of a carbon nitride polymer. *Chem. Eur. J.* **13**, 4969–4980 (2007)
 15. Y. Wang, X. Wang, M. Antonietti, Polymeric graphitic carbon nitride as a heterogeneous organocatalyst: from photochemistry to multipurpose catalysis to sustainable chemistry. *Angew. Chem. Int. Ed.* **43**, 68–89 (2012)
 16. P. Murugesan, S. Narayanan, M. Manickam, Experimental studies on photocatalytic reduction of CO₂ using AgBr decorated g-C₃N₄ composite in TEA mediated system. *J CO₂ Util.* **22**, 250–261 (2017)
 17. H. Wang, Y. Xu, L. Jing, S. Huang, Y. Zhao, M. He, H. Xu, H. Li, Novel magnetic BaFe₁₂O₁₉/g-C₃N₄ composites with enhanced thermocatalytic and photo-Fenton activity under visible-light. *J. Alloys Compd.* **710**, 510–518 (2017)
 18. S.B. Kokane, R. Sasikala, D.M. Phase, S.D. Sartale, In₂S₃ nanoparticles dispersed on g-C₃N₄ nanosheets: role of heterojunctions in photoinduced charge transfer and photoelectrochemical and photocatalytic performance. *J. Mater. Sci.* **52**, 1–14 (2017)
 19. R. Sun, Q. Shi, M. Zhang, L. Xie, J. Chen, X. Yang, M. Chen, W. Zhao, Enhanced photocatalytic oxidation of toluene with a coral-like direct Z-scheme BiVO₄/g-C₃N₄ photocatalyst. *J. Alloys Compd.* **714**, 619–626 (2017)
 20. X. Chen, D.H. Kuo, Y.X. Hou, Enhancing the photodegradation of charged pollutants under visible light in Ag₂O/g-C₃N₄ catalyst by Coulombic interaction. *J. Mater. Sci.* **52**, 5147–5154 (2017)
 21. Y. Yuan, G.F. Huang, W.Y. Hu, D.N. Xiong, B.X. Zhou, S. Chang, W.Q. Huang, Construction of g-C₃N₄/CeO₂/ZnO ternary photocatalysts with enhanced photocatalytic performance. *J. Phys. Chem. Solids* **106**, 1–9 (2017)
 22. J. Chen, X. Xiao, Y. Wang, Z. Ye, Fabrication of hierarchical sheet-on-sheet WO₃/g-C₃N₄ composites with enhanced photocatalytic activity. *J. Alloys Compd.* **777**, 325–334 (2019)
 23. W. Chen, Z.-C. He, G.-B. Huang, C.-L. Wu, W.-F. Chen, X.-H. Liu, Direct Z-scheme 2D/2D MnIn₂S₄/g-C₃N₄ architectures with highly efficient photocatalytic activities towards treatment of pharmaceutical wastewater and hydrogen evolution. *Chem. Eng. J.* **359**, 244–253 (2019)
 24. Q. Wang, K. Wang, L. Zhang, H. Wang, W. Wang, Photocatalytic reduction of CO₂ to methane over PtOx-loaded ultrathin Bi₂WO₆ nanosheets. *Appl. Surf. Sci.* **470**, 832–839 (2019)
 25. X. Shi, P. Wang, W. Li, Y. Bai, H. Xie, Y. Zhou, L. Ye, Change in photocatalytic NO removal mechanisms of ultrathin BiOBr/BiOI via NO₃⁻ adsorption. *Appl. Catal. B* **243**, 322–329 (2019)
 26. H. Li, Y. Chen, W. Zhou, H. Gao, G. Tian, Tuning in BiVO₄/Bi₄V₂O₁₀ porous heterophase nanospheres for synergistic photocatalytic degradation of organic pollutants. *Appl. Surf. Sci.* **470**, 631–638 (2019)
 27. L.S. Zhang, H.L. Wang, Z.G. Chen, P.K. Wong, J.S. Liu, Bi₂WO₆ micro/nano-structures: synthesis, modifications and visible-light-driven photocatalytic applications. *Appl. Catal. B.* **106**, 1–13 (2011)
 28. Y. Zhang, J. Lu, M.R. Hoffmann, Q. Wang, Y. Cong, Q. Wang, H. Jin, Synthesis of g-C₃N₄/Bi₂O₃/TiO₂ composite nanotubes: enhanced activity under visible light irradiation and improved photoelectrochemical activity. *RSC Adv.* **5**, 48983–48991 (2015)
 29. G. Zhu, M. Hojamberdiev, S. Zhang, S.T.U. Din, W. Yang, Enhancing visible-light-induced photocatalytic activity of BiOI microspheres for NO removal by synchronous coupling with Bi metal and graphene. *Appl. Surf. Sci.* **467–468**, 968–978 (2019)
 30. J. Zhong, J. Li, X. Liu, Q. Wang, H. Yang, W. Hu, C. Cheng, J. Song, M. Li, T. Jin, Enhanced photo-induced charge separation and solar-driven photocatalytic activity of g-C₃N₄ decorated by SO₄²⁻. *Mater. Sci. Semicond. Process.* **40**, 508–515 (2015)
 31. K. Dai, L. Lu, C. Liang, G. Zhu, Q. Liu, L. Geng, J. He, A high efficient graphitic-C₃N₄/BiOI/graphene oxide ternary nanocomposite heterostructured photocatalyst with graphene oxide as electron transport buffer material. *Dalton Trans.* **44**, 7903–7910 (2015)
 32. Z. Jiang, X. Liang, Y. Liu, T. Jing, Z. Wang, X. Zhang, X. Qin, Y. Dai, B. Huang, Enhancing visible light photocatalytic degradation performance and bactericidal activity of BiOI via ultrathin-layer structure. *Appl. Catal. B* **211**, 252–257 (2017)
 33. M. Pirhashemi, A. Habibi-Yangjeh, Simple and large scale one-pot method for preparation of AgBr–ZnO nanocomposites as highly efficient visible light photocatalyst. *Appl. Surf. Sci.* **283**, 1080–1088 (2013)
 34. S.C. Yan, Z.S. Li, Z.G. Zou, Photodegradation of rhodamine B and methyl orange over boron-doped g-C₃N₄ under visible light irradiation. *Langmuir* **26**, 3894–3901 (2010)
 35. L. Ye, J. Liu, Z. Jiang, T. Peng, L. Zan, Facets coupling of BiOBr-g-C₃N₄ composite photocatalyst for enhanced visible-light-driven photocatalytic activity. *Appl. Catal. B* **142**, 1–7 (2013)
 36. J.C. Wang, H.C. Yao, Z.Y. Fan, L. Zhang, J.S. Wang, S.Q. Zang, Z.J. Li, Indirect Z-Scheme BiOI/g-C₃N₄ photocatalysts with enhanced photoreduction CO₂ activity under visible light irradiation. *ACS Appl. Mater. Interfaces* **8**, 3765–3775 (2016)
 37. Z. You, C. Wu, Q. Shen, Y. Yu, H. Chen, Y. Su, H. Wang, C. Wu, F. Zhang, H. Yang, A novel efficient g-C₃N₄@BiOI p-n heterojunction photocatalyst constructed through the assembly of g-C₃N₄ nanoparticles. *Dalton Trans.* **47**, 7353–7361 (2018)
 38. S. Ning, H. Lin, Y. Tong, X. Zhang, Q. Lin, Y. Zhang, J. Long, X. Wang, Dual couples Bi metal depositing and Ag@AgI islanding on BiOI 3D architectures for synergistic bactericidal mechanism of *E. coli* under visible light. *Appl. Catal. B.* **204**, 1–10 (2017)

39. X. Zhou, C. Shao, X. Li, X. Wang, X. Guo, Y. Liu, Three dimensional hierarchical heterostructures of g-C₃N₄ nanosheets/TiO₂ nanofibers: controllable growth via gas-solid reaction and enhanced photocatalytic activity under visible light. *J. Hazard. Mater.* **344**, 113–122 (2017)
40. J. Cao, B. Xu, H. Lin, B. Luo, S. Chen, Novel heterostructured Bi₂S₃/BiOI photocatalyst: facile preparation, characterization and visible light photocatalytic performance. *Dalton Trans.* **41**, 11482–11490 (2012)
41. J. Deli, C. Linlin, Z. Jianjun, C. Min, S. Weidong, X. Jimin, Novel p-n heterojunction photocatalyst constructed by porous graphite-like C₃N₄ and nanostructured BiOI: facile synthesis and enhanced photocatalytic activity. *Dalton Trans.* **42**, 15726–15734 (2013)
42. J. Oh, J.M. Lee, Y. Yoo, J. Kim, S.J. Hwang, S. Park, New insight of the photocatalytic behaviors of graphitic carbon nitrides for hydrogen evolution and their associations with grain size, porosity, and photophysical properties. *Appl. Catal. B* **218**, 349–358 (2017)
43. R. Hao, X. Xiao, X. Zuo, J. Nan, W. Zhang, Efficient adsorption and visible-light photocatalytic degradation of tetracycline hydrochloride using mesoporous BiOI microspheres. *J. Hazard. Mater.* **209–210**, 137–145 (2012)
44. X. Zhang, L. Zhang, T. Xie, D. Wang, Low-temperature synthesis and high visible-light-induced photocatalytic activity of BiOI/TiO₂ heterostructures. *J. Phys. Chem. C* **113**, 7371–7378 (2009)
45. K. Santosh, T. Surendar, B. Arabinda, K. Bharat, S. Vishnu, Synthesis of novel and stable g-C₃N₄/N-doped SrTiO₃ hybrid nanocomposites with improved photocurrent and photocatalytic activity under visible light irradiation. *Dalton Trans.* **43**, 16105–16114 (2014)
46. Z. Xiu, H. Bo, Y. Wu, X. Hao, Graphite-like C₃N₄ modified Ag₃PO₄ nanoparticles with highly enhanced photocatalytic activities under visible light irradiation. *Appl. Surf. Sci.* **289**, 394–399 (2014)
47. S. Wan, M. Ou, W. Cai, S. Zhang, Q. Zhong, Preparation, characterization, and mechanistic analysis of BiVO₄/CaIn₂S₄ hybrids that photocatalyze NO removal under visible light. *J. Phys. Chem. Solids* **122**, 239–245 (2018)
48. Q. Xiang, J. Yu, M. Jaroniec, Preparation and enhanced visible-light photocatalytic H₂-production activity of graphene/C₃N₄ composites. *J. Phys. Chem. C* **115**, 7355–7363 (2011)
49. Y. Zhang, J. Wu, Y. Deng, Y. Xin, H. Liu, D. Ma, N. Bao, Synthesis and visible-light photocatalytic property of Ag/GO/g-C₃N₄ ternary composite. *J. Mater. Sci. Eng. B* **221**, 1–9 (2017)
50. S.C. Yan, Z.S. Li, Z.G. Zou, Photodegradation performance of g-C₃N₄ fabricated by directly heating melamine. *Langmuir* **25**, 10397–10401 (2009)
51. J. Di, J. Xia, S. Yin, H. Xu, L. Xu, Y. Xu, M. He, H. Li, Preparation of sphere-like g-C₃N₄/BiOI photocatalysts via a reactable ionic liquid for visible-light-driven photocatalytic degradation of pollutants. *J. Mater. Chem. A* **2**, 5340–5351 (2014)
52. V. Vaiano, M. Matarangolo, J.J. Murcia, H. Rojas, J.A. Navío, M.C. Hidalgo, Enhanced photocatalytic removal of phenol from aqueous solutions using ZnO modified with Ag. *Appl. Catal. B* **225**, 197–206 (2018)
53. J. Zhang, Q. Zhou, L. Ou, Kinetic, isotherm, and thermodynamic studies of the adsorption of methyl orange from aqueous solution by chitosan/alumina composite. *J. Chem. Eng. Data* **57**, 412–419 (2012)
54. C. Cai, H. Zhang, X. Zhong, L. Hou, Ultrasound enhanced heterogeneous activation of peroxydisulfate by a bimetallic Fe-Co/SBA-15 catalyst for the degradation of Orange II in water. *J. Hazard. Mater.* **283**, 70–79 (2015)
55. M. Karimi-Shamsabadi, M. Behpour, A.K. Babaheidari, Z. Saberi, Efficiently enhancing photocatalytic activity of NiO-ZnO doped onto nanozeoliteX by synergistic effects of p-n heterojunction, supporting and zeolite nanoparticles in photodegradation of Eriochrome Black T and Methyl Orange. *J. Photochem. Photobiol. A* **346**, 133–143 (2017)
56. A. Nezamzadeh-Ejhi, M. Karimi-Shamsabadi, Decolorization of a binary azo dyes mixture using CuO incorporated nanozeolite-X as a heterogeneous catalyst and solar irradiation. *Chem. Eng. J.* **228**, 631–641 (2013)

Publisher's Note Springer Nature remains neutral with regard to jurisdictional claims in published maps and institutional affiliations.